# Magnetization reversal induced by antiphase domain boundaries in Ni$_2$MnZ Heusler compounds

Ulrike Zweck [1,*] Pascal Neibecker,[1] Sebastian Mühlbauer,[1] Qiang Zhang [2] Pin-Yi Chiu,[1] and Michael Leitner [1,†]

[1]*Heinz Maier-Leibnitz Zentrum (MLZ), Technische Universität München, 85747 Garching, Germany*
[2]*Oak Ridge National Laboratory, 1 Bethel Valley Rd., Oak Ridge, Tennessee 37830, USA*

The correlation of the microstructure and the magnetic properties of Ni$_2$MnAl$_{0.5}$Ga$_{0.5}$ and Ni$_2$MnAl Heusler alloys is studied in samples of distinct L2$_1$ order states by neutron powder diffraction and small-angle scattering. The extracted correlation lengths of the structural and magnetic order agree over all annealing states, which implies the structural antiphase domain boundaries to be identical to the magnetic domain walls, and thus to inherently give rise to a magnetization reversal. The findings are discussed in the context of recent small-angle neutron scattering studies on related systems, and their wider implications are pointed out.

## I. INTRODUCTION

Structural order has often a crucial effect on system properties such as magnetism or yield strength, for example, in superalloys (e.g., Ni$_3$Al [1]) and functional materials such as the Heusler alloys [2]. Specifically in compounds where the magnetic moments are mainly carried by Mn atoms, such as MnAl or Ni$_2$MnZ compounds [3–5], the arrangement of the Mn atoms is vital for the magnetic properties via the strongly distance-dependent magnetic interaction [4]. When cooling from the disordered phase, the growth of the superstructure from independent nuclei results in the formation of antiphase domains (APDs). At the boundaries of these domains, the assignment of elements to sublattices displays breaks, and their influence on magnetic properties has been studied in various ordered compounds [3,6–8]. For example in the compound MnAl, antiphase domain boundaries have long been considered to give rise to magnetic domain interfaces [3] with a reversal of magnetization.

In contrast to the ferromagnetic behavior of fully L2$_1$-ordered Ni$_2$MnGa [9], Ni$_2$MnAl is typically found to be antiferromagnetic [4,10], which is explained as a consequence of its B2 order [11]. How the microstructure in Ni$_2$MnZ compounds is correlated with the magnetic behavior remains an open and heavily investigated question in the community [5,7,12–14]. A critical observation by electron microscopy in this context is that the APD boundaries between L2$_1$ ordered domains often coincide with the magnetic domain interfaces [7,12,13], which has a decisive effect on the macroscopic magnetic properties [15,16]. To explain this behavior, there

are two possibilities: On the one hand, there is the scenario realized in a typical ferromagnet such as iron, where the magnetic domain structure forms as a compromise of the short-range exchange interaction (favoring parallel alignment of the moments) and the long-range dipole-dipole interaction (favoring antiparallel alignment), with a characteristic scale of tens to hundreds of $\mu$m [17]. Such domain walls can easily get pinned at structural defects where magnetic exchange interactions are locally disturbed or absent. On the other hand, it is conceivable that, beyond merely pinning magnetic domain walls whose existence is mandated by the magnetostatic interaction, antiphase domain boundaries actively induce magnetic domain walls: in the model of Zijlstra and Haanstra for MnAl [3] or Lapworth and Jakubovics for Cu$_2$MnAl [6], the Mn moments' strongly distance-dependent magnetic interaction directly leads to a reversal of magnetization at the APD boundary, where antiferromagnetically interacting Mn-Mn nearest-neighbor pairs can exist. The relatively small scale of the magnetic domains in Ni$_2$MnZ Heusler compounds, particularly in as-quenched conditions [7], points towards the latter mechanism, while the discussion in the community typically is in terms of the concept of defect pinning [7,12,13,18,19].

In addition to structural order, neutron scattering can access also a sample's magnetic microstructure due to the coupling of the neutron's magnetic moment to the local internal magnetic fields. In diffraction experiments the finite correlation length of structural order results in a broadening of the corresponding structural peaks, with the characteristic domain size being directly linked to the peak's full width at half maximum (FWHM) via the Scherrer equation [20]. A microstructured ferromagnet can be investigated via small-angle neutron scattering (SANS) [21–23], where the contrast between the local magnetic fields, corresponding to structures of 1 nm up to a few hundred nm yields an additional scattering at low wave vector transfers in the magnetically ordered phase.

The aim of this study is to investigate how the microscopic antiphase domain configuration is correlated with the magnetic microstructure of the Ni$_2$MnZ Heusler alloys.

*ulrike.zweck@frm2.tum.de
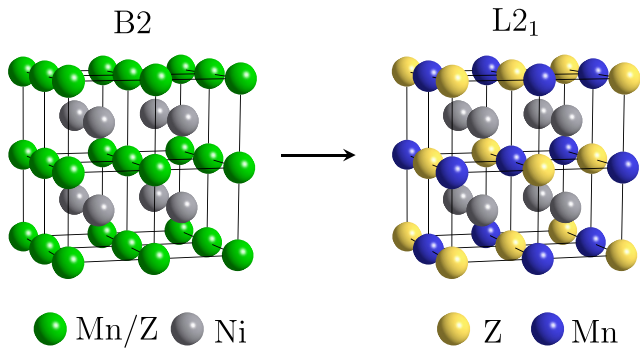†michael.leitner@frm2.tum.de

FIG. 1. Schematic representations of the ordering states of Ni$_2$MnZ on the bcc lattice: B2 order can be described by two sc sublattices, with Ni atoms occupying one sublattice while Mn and Z atoms occupy in disorder the other one. In the L2$_1$ structure further ordering occurs on the latter sublattice.

Specifically, we want to settle the question raised above, namely, whether a structural antiphase domain wall merely traps magnetic domain walls, or whether it directly induces a magnetization reversal. The latter scenario would imply a one-to-one correspondence between structural and magnetic domains as long as the APDs are smaller than the magnetic domain length scale as determined by magnetostatics. In Ni$_2$MnGa, the B2 structure transforms within seconds to the full-Heusler structure [24], whereas Ni$_2$MnAl shows in general a low L2$_1$-order tendency [4]. Intermediate quaternary compositions allow us to access different states of order as mirrored in the magnetic properties when quenching from the B2 regime and annealing subsequently at low temperatures where the L2$_1$ order is stable [15,16]. In this article we study Ni$_2$MnAl and Ni$_2$MnAl$_{0.5}$Ga$_{0.5}$ samples at various annealing conditions corresponding to different degrees of long-range order and antiphase domain sizes via neutron powder diffraction and small-angle neutron scattering. We compare the correlation lengths of structural and magnetic order and discuss the small-angle signal's evolution around the magnetic phase transition.

## II. CRYSTAL STRUCTURES

Ternary Heusler systems can show a multitude of structural ordering transitions. While in an early study the existence of a totally disordered A2 phase has been reported for the Ni$_2$MnAl composition [25] (see, however, the conflicting data of Ref. [26]), for the conditions of our study at least B2 order is realized for both compositions. This superstructure on the body-centered lattice is depicted in Fig. 1 and is defined by the space group 221 (Pm$\bar{3}$m) with the Ni atoms congregating on the sublattice of the body-centered positions, corresponding to the Wyckoff positions (1$b$) at (1/2, 1/2, 1/2), while the Mn and Al atoms occupy randomly the Wyckoff positions (1$a$) at (0,0,0).

At 774 K, Ni$_2$MnAl transforms to the fully ordered L2$_1$ structure [27]. At this transition, the previously disordered Mn and Al atoms start to arrange in a regular order. As a consequence, the crystal symmetry changes to the space group 225 (Fm$\bar{3}$m), where the former Wyckoff positions (1$a$)

TABLE I. Composition of the Ni$_2$MnAl$_{0.5}$Ga$_{0.5}$ and Ni$_2$MnAl ingots measured via EDS.

|  | Ni | Mn | Al | Ga |
|---|---|---|---|---|
| Ni$_2$MnAl$_{0.5}$Ga$_{0.5}$ | 51.1 | 26.0 | 11.2 | 11.7 |
| Ni$_2$MnAl | 49.2 | 25.6 | 25.2 |  |

decompose into the Wyckoff positions (4$a$) at (0,0,0) and (4$b$) at (1/2, 1/2, 1/2), occupied by Al and Mn, respectively. The Wyckoff positions (8$c$) at (1/4, 1/4, 1/4) and equivalent positions remain being occupied by Ni atoms, as depicted on the right in Fig. 1. The quaternary compound Ni$_2$MnAl$_{0.5}$Ga$_{0.5}$ shows an analogous behavior, but the addition of Ga atoms results in a stronger L2$_1$ ordering tendency and thus a higher B2-L2$_1$ ordering temperature of 931 K [15].

## III. SAMPLE PREPARATION AND CHARACTERIZATION

Polycrystalline Ni$_2$MnAl and Ni$_2$MnAl$_{0.5}$Ga$_{0.5}$ ingots were prepared by induction melting and tilt or suction casting of high-purity elements under an Ar atmosphere. To promote homogeneity and remove segregation effects from casting, the ingots subsequently underwent a solution annealing treatment. The ingots' actual composition was determined by energy-dispersive x-ray spectroscopy (EDS) at the Staatliche Materialprüfamt für Maschinenbau at the Technical University of Munich, Germany. For each alloy ten positions were studied. The averages over these values are given in Table I and show a satisfactory agreement with the nominal compositions. The ingots were ground to a powder of diameter smaller than 125 $\mu$m. A well-defined stress-free initial state was defined by annealing the powders in the B2 regime at 1073 K for 4 h encapsulated in evacuated quartz glass ampoules and quenching in water. To obtain distinct degrees of L2$_1$ order and antiphase domain sizes, the powder was partitioned and subjected to a low-temperature annealing treatment in the L2$_1$ regime at 623 K, with the Ni$_2$MnAl$_{0.5}$Ga$_{0.5}$ samples being annealed for 0.5 h, 3 h, and 10 d, and the Ni$_2$MnAl samples for 24 h and 10 d, respectively. For both compositions an as-quenched (a.q.) sample was retained.

The magnetic transition temperatures $T_c$ of these samples were determined by differential scanning calorimetry (DSC) measurements at heating rates of 10 K/min. For checking whether the grinding process had any influence on the samples' magnetic properties, corresponding bulk samples were prepared and investigated via DSC after repeated annealing steps at 623 K. The data were recorded in a temperature range between 250 and 400 K. While the data obtained on the bulk samples show for the second-order magnetic transition a quite distinct step-like curve with a well-defined transition temperature, the DSC curves recorded for the powder samples are in general broader and less distinctive, most probably due to surface effects in the powder grains. Thus, the data were convolved with a centered Gaussian kernel with $\sigma = 4$ K and the magnetic transition temperature was identified as the position of the extremal gradient of the resulting smoothed curve. The retrieved transition temperatures $T_c$ are displayed in Fig. 2 and reported in Table II and show, as expected [28],
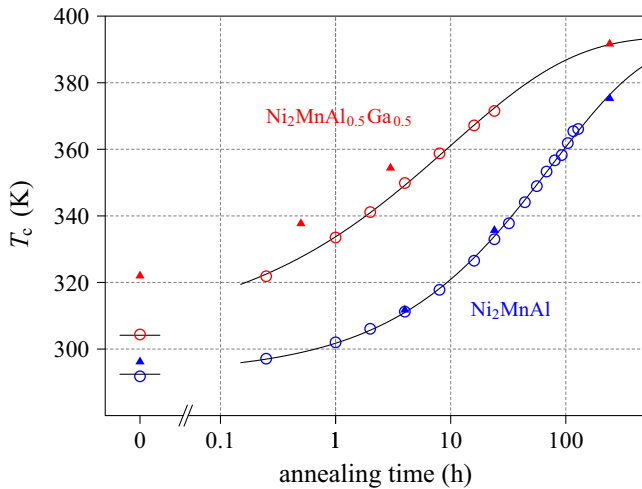
FIG. 2. Evolution of the magnetic transition temperature with annealing at 623 K for the $Ni_2MnAl$ and $Ni_2MnAl_{0.5}Ga_{0.5}$ powder (filled triangles) and bulk (empty circles) samples. The black curves are phenomenological fits.

an increase with annealing time for both alloys. For $Ni_2MnAl$, the evolution of the bulk and powder samples are in excellent agreement, while for $Ni_2MnAl_{0.5}Ga_{0.5}$, the retrieved values for the powder samples are in general higher than those of the bulk samples. This deviation is likely a consequence of the transition temperature's phenomenological determination due to the broadened DSC curves of the powder samples.

## IV. NEUTRON POWDER DIFFRACTION

To study the length scale of $L2_1$ order in these compounds, neutron powder diffraction studies were performed on the time-of-flight diffractometer POWGEN [29] at the Spallation Neutron Source (SNS), Oak Ridge, USA. The powder samples were encapsulated in vanadium cans and measured at 450 K using two center wavelengths $\lambda_c = 1.333$ Å and 2.665 Å at a bandwidth $\Delta\lambda$ of 1 Å and a pulse rate of 60 Hz. The acquisition time per pattern was approximately 15 min. Since all samples have magnetic transition temper-

TABLE II. DSC-derived magnetic transition temperatures, APD boundary density $L_{struc}$ as well as magnetic interface density $L_{mag}$ of the $Ni_2MnAl_{0.5}Ga_{0.5}$ and $Ni_2MnAl$ samples of distinct annealing durations at 623 K. Missing values are due to $Ni_2MnAl$ not having been measured by SANS in the state after 24 h annealing, and undetectable superstructure peaks and magnetic small-angle scattering for as-quenched $Ni_2MnAl$ due to vanishing long-range order.

| $Ni_2MnAl_{0.5}Ga_{0.5}$ | As-quenched | 0.5 h | 3 h | 10 d |
|---|---|---|---|---|
| $T_c$ (K) | 322 | 338 | 354 | 392 |
| $L_{struc}$ (nm) | 3.7 | 3.6 | 4.8 | 11.9 |
| $L_{mag}$ (nm) | 6.0 | 4.4 | 5.3 | 13.2 |
| $Ni_2MnAl$ | As-quenched | 24 h | 10 d | |
| $T_c$ (K) | 296 | 336 | 375 | |
| $L_{struc}$ (nm) | – | 2.5 | 7.5 | |
| $L_{mag}$ (nm) | – | – | 9.6 | |

atures below 400 K, we expected to observe mainly nuclear scattering in the diffraction patterns. The structural details were extracted by employing the Pawley refinement method [30], simultaneously fitting the data from both wavelengths with common sample parameters. The instrumental resolution function was approximated by a convolution of back-to-back exponentials with a pseudo-Voigt function [31].

Figure 3 shows the neutron powder diffraction patterns of the four $Ni_2MnAl_{0.5}Ga_{0.5}$ samples and the three $Ni_2MnAl$ samples, in both cases with $\lambda_c = 2.665$ Å. The diffraction data were corrected for absorption. For an $L2_1$ ordered structure the nonzero Bragg reflections are those for which the Miller indices are either all even or all odd. The reflections can be divided into three distinct peak families: First, if $h$, $k$, and $l$ are all odd, the reflection is due to the different scattering lengths on the (4a) and (4b) sites; that is, the $L2_1$ superstructure. If $h$, $k$, and $l$ are all even, one has to differentiate: If the Miller indices' sum is not a multiple of four, its structure factor results from the diffraction contrast between the Wyckoff positions (8c) on the one hand and (4a) and (4b) on the other hand, which results already from B2 ordering. If $h$, $k$, and $l$ sum to a multiple of four, it is a primitive peak of the underlying bcc (A2) lattice with a structure factor that depends solely on the alloys' composition, resulting from all lattice sites contributing in phase. In our measured data, the primitive and the B2 superstructure peaks are for every annealing state as sharp as those from calibration samples, without any indication of strain or size broadening beyond the experimental resolution. Thus, we can use these peaks to fit a set of parameters describing the instrumental resolution function optimally for our measurements.

In contrast to the primitive and B2 superstructure peaks, the odd-order $L2_1$ superstructure peaks are noticeably broadened compared with the instrumental resolution. As a function of increasing annealing time all theses peaks sharpen and gain intensity. For a given sample state, this broadening does not vary with $Q$, implying that it results from a finite correlation length of the associated order; that is, from an antiphase domain structure of the $L2_1$ superstructure. Thus, the observed sharpening of the $L2_1$ superstructure peaks with annealing duration is a direct indication of the antiphase domains' coarsening.

For a quantitative analysis of the $L2_1$ correlation length with the annealing time we employed whole-pattern Pawley refinement. We assume only resolution-broadened peak profiles for the primitive and B2 superstructure peaks, while the additional inherent broadening of the $L2_1$ reflections is described by an appropriate model function as derived in Ref. [32] from the coarsening of APDs by Monte Carlo simulations. To describe the real-space correlation functions a model function scaled by a time-dependent parameter $L$ was proposed. The resulting expression for a peak profile in powder diffractometry is given by

$$S'(k_x) = \frac{8\pi^2}{k_x^2 + 1/b^2} + \sqrt{32\pi^5} \sum_{i=1}^{2} a_i \sigma_i \exp\left(-k_x^2 \sigma_i^2 / 2\right), \quad (1)$$

with $k_x = (Q - Q_{peak})L_{struc}(t)/2$ and $Q_{peak}$ being the peak position. The parameters $b$, $a_i$, and $\sigma_i$ for $i \in \{1, 2\}$ are given in Ref. [32].
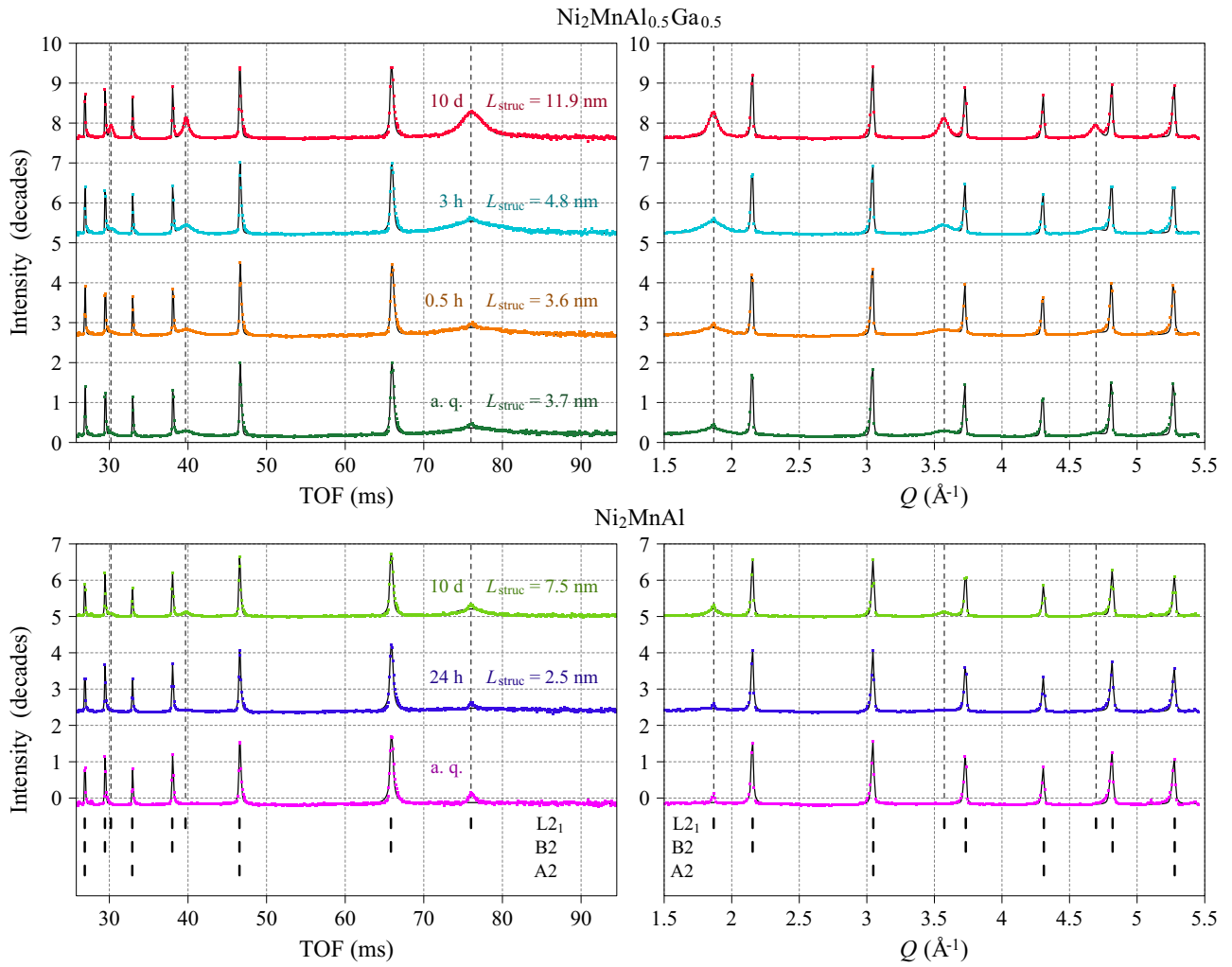
FIG. 3. Neutron diffraction pattern obtained on $Ni_2MnAl_{0.5}Ga_{0.5}$ (top) and $Ni_2MnAl$ (bottom) after distinct annealing durations at 450 K measured at $\lambda_c = 2.665$ Å together with Pawley refinements as solid black curves. The peak locations for the different states of order (A2, B2, and $L2_1$) are marked, and the broadened $L2_1$ superstructure peaks additionally indicated by the dashed lines. On the left side the patterns are depicted as measured dependent on the time of flight, while on the right side the data and models are transformed to $Q$ space. The intensity axis uses a logarithmic scale, with distinct plots shifted by two and a half decades.

The fitted scale of the APDs $L_{struc}(t)$ is inversely proportional to the interfacial density of the domains and is equivalent to the scale obtained by the linear intercept method [33] applied in microscopy experiments. To describe the background we use a polynomial of degree five. We minimize the squared deviations between the diffraction data and the fit function, weighted according to the counting statistics. Even though the measurements were performed well above the magnetic transition temperatures, possible magnetic short-range order can cause an additional intensity contribution particularly at low $Q$ due to the magnetic form factor's strong decrease with $Q$, which is most conspicuously visible for $Ni_2MnAl$ in the as-quenched condition and can be rationalized by its known antiferromagnetic ground state [10]. Thus the first $L2_1$ superstructure peak is neglected in the refinement and does not contribute to the determination of the structural length scale $L_{struc}$.

As can be seen in Fig. 3, the data can be fit very well with our model. In itself, this would not be remarkable, as the convolution with the instrumental resolution function hides

the details of the assumed inherent broadening. The virtue of our approach lies in the quantitative accuracy, with the fitted antiphase domain length scales $L_{struc}$ as given in Table II being only due to the inherent broadening. As expected, they show an increase with annealing time, with $Ni_2MnAl_{0.5}Ga_{0.5}$ having generally larger domains at a given annealing condition than $Ni_2MnAl$. This parallels the results of Ref. [16], where higher annealing temperatures resulted in a correspondingly faster growth of the domain size. Note that as-quenched $Ni_2MnAl$ displays only structural peaks corresponding to B2 order, prohibiting the assignment of an $L2_1$ antiphase domain length scale.

## V. SMALL-ANGLE NEUTRON SCATTERING

While crystalline periodicity gives diffraction peaks in the wide-angle region and finite correlation lengths of crystalline order lead to their broadening, variations of the mean scattering length density on the mesoscopic length scale give rise to small-angle neutron scattering (SANS). The neutron's
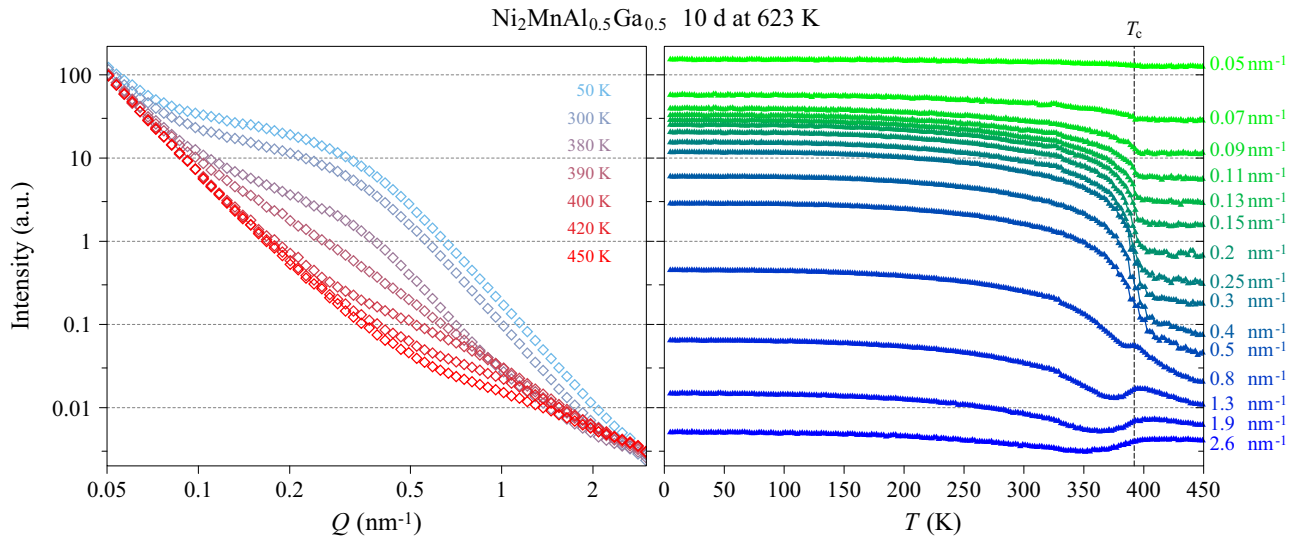
FIG. 4. Temperature-dependent magnetic small-angle neutron scattering of the $Ni_2MnAl_{0.5}Ga_{0.5}$ sample 10 d annealed at 623 K. Left: SANS signals for distinct temperatures. Right: SANS intensity for distinct $Q$ as function of temperature, with DSC-derived magnetic transition temperature $T_c$ indicated.

magnetic moment couples to the local internal magnetic field, thus a magnetic microstructure can be probed by SANS experiments. Such measurements have been conducted at SANS-1 at the FRM II, Garching [34,35]. For suppressing multiple scattering the powder samples were encapsulated between aluminium foil, giving an effective sample thickness of 0.4 mm. Measurements between 4.2 and 450 K were performed using unpolarized neutrons at detector distances of 2 and 8 m at a neutron wavelength of 5 Å and at a detector distance of 20 m with a wavelength of 6 Å in order to access even smaller $Q$. To match the incident divergence to the detector resolution, the distance from the neutron guide exit to the sample was set equal to the sample-detector distance by inserting neutron guide elements down to a minimum distance of 4 m, where the critical angle of reflection in the neutron guide starts to limit the achievable divergence. The isotropic scattering signal was radially averaged to obtain the scattering profile over the range of $0.02\,\text{nm}^{-1} \leqslant Q \leqslant 4.2\,\text{nm}^{-1}$. The data were collected continuously during temperature sweeps with cooling and heating rates of 2 K/min, read out once per minute. Thus, our nominal temperatures actually correspond to windows of 2 K. The data are corrected to the beam monitor, and as we used equal sample volumes, they are therefore proportional to the structure factor $S(Q)$ per formula unit irrespective of the composition.

Figure 4 displays the evolution of the SANS profiles with temperature for the $Ni_2MnAl_{0.5}Ga_{0.5}$ sample at the longest annealing state of 10 h. At low $Q$ the profiles can be best described by a straight line on these log-log plots, indicating a decay of intensity with $Q^{-4}$ that does not change with temperature. The main contributions to this signal are the divergence of the incident neutron beam as well as the Porod scattering from interfaces such as powder grain surfaces and grain boundaries [36]. As the temperature is lowered through the magnetic transition at 392 K, a distinctive shoulder develops around $Q \approx 0.3\,\text{nm}^{-1}$ due to the emergence of magnetically ordered domains. At the highest measured $Q$ beyond 1 nm$^{-1}$, the data show a peculiar behavior in this temperature region:

with falling temperature, they first rise, reach a maximum around the transition temperature, display an intermittent regime of decreasing intensity, and finally increase again. In agreement with Refs. [21] and [37], we interpret this part of the signal as scattering due to short-range order of the spins in the paramagnetic regime, which has a maximum at the transition temperature.

The shoulder due to local variations in the magnetization on the nm scale is present in all annealing states of $Ni_2MnAl_{0.5}Ga_{0.5}$ as well as in annealed $Ni_2MnAl$, as depicted in Fig. 5. At a given temperature, the additional contribution is strongest for the samples with the longest annealing. Also its position in $Q$ varies noticeably, moving to smaller $Q$ with progressive annealing. Different from the other samples, $Ni_2MnAl$ in the as-quenched state does not show magnetic small-angle scattering. Thus, in this case the B2 state can be retained by quenching, leading to a conventional antiferromagnetic state at low temperatures, in agreement with Ref. [10].

According to our hypothesis of a one-to-one correspondence of structural and magnetic domains, the magnetic small-angle scattering should be described by the same real-space correlation function as the broadening of the superstructure peaks. Thus, for modeling the corresponding contribution to the scattering we use the model function parametrized by our Monte Carlo simulations [32], but now in its formulation for a point-wise evaluation of the intensity in three-dimensional reciprocal space, where the previously used expression for the diffraction peak profile was the orthogonal projection of the intensity onto a line through a superstructure peak. It is given as

$$S(k) = \frac{8\pi}{(k^2 + 1/b^2)^2} + \sqrt{8\pi^3} \sum_{i=1}^{2} a_i \sigma_i^3 \exp\left(-k^2 \sigma_i^2/2\right), \quad (2)$$

with $k = QL_{\text{mag}}(t)/2$. Contrary to the case of diffraction, in SANS typically systematic deficiencies of the peak model are the main sources of deviations due to the higher statistics
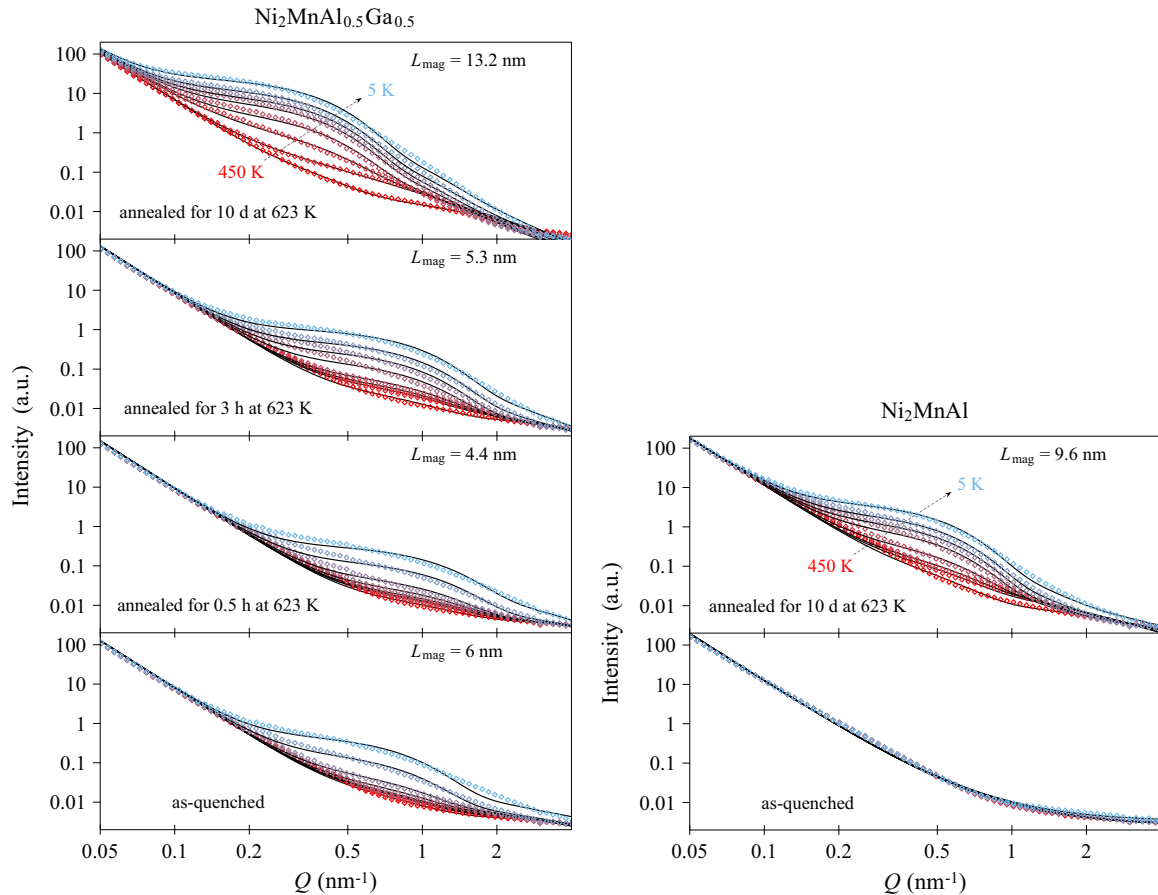
FIG. 5. Temperature-dependent SANS profiles in the temperature range for $Ni_2MnAl_{0.5}Ga_{0.5}$ (left) and $Ni_2MnAl$ (right) in various annealing states, in each case measured at 5, 300, 340, 360, 380, 390, 400, and 450 K, and modeled according to Eq. (3).

and better resolution. Thus, our objective function in fitting is the nonweighted sum of squared *relative* deviations between data and model, which corresponds to minimizing the visual deviations in a log-log plot.

Including the above-mentioned $Q^{-4}$ contribution and the Lorentzian contribution due to magnetic short-range order, the complete fit function is given as

$$\frac{d\Sigma}{d\Omega} = C(T)Q^{-4} + A(T)L_{mag}^3 S(QL_{mag}/2) + \frac{B(T)\Gamma(T)}{Q^2 + \Gamma(T)^2},$$

(3)

where the prefactor $A(T)$ is a measure of the strength of the magnetic small-angle signal $S(k)$, while $B(T)$ and $\Gamma(T)$ are the Lorentzian's strength and width, respectively. We assume a magnetic domain scale $L_{mag}$ that is independent of temperature—for reasons of stability we determined it by fitting the profiles recorded at low temperatures ($T < 100$ K).

As can be seen in Fig. 5, our model function's fit to the small-angle scattering signal is in general quite good, considering that apart from prefactor and scale there are no free parameters to describe its shape. Discernible deviations seem to be due to the experimental signal being somewhat broader in $Q$. Such a behavior would follow from a spatial inhomogeneity of the characteristic domain length scale, perhaps due to composition fluctuations, but our present data do not allow us to give a definitive explanation.

The fitted length scales $L_{mag}$ for the different samples are listed in Table II. The consistent definition of structural and magnetic length scale allows us to directly compare the respective domain structures. Indeed, for a given system and annealing state the two agree quite closely, and the absence of $L2_1$ structural order and associated antiphase domains in as-quenched $Ni_2MnAl$ is reflected in the nonexistent corresponding magnetic small-angle signal. Thus, we think that it is safe to accept our hypothesis that magnetic domain walls do not merely get pinned at antiphase domain boundaries, in which case the magnetic domain interface density could be significantly larger or smaller than the antiphase domain interface density, but that the structural domain boundaries inherently induce a magnetic domain boundary. A further argument for the strict coincidence is that, as the samples are annealed and thus the structural domain interface density decreases, so does the magnetic domain interface density, which cannot be explained in another way. Our measurements show that the magnetic scale is, if at all different, slightly larger than the structural scale, therefore we can also exclude the possibility of gradual rotations of the magnetization within APDs, which should rather give rise to smaller fitted length scales of the magnetic domains. Note that the described scenario applies particularly for our case of quite small APD sizes and a concomitantly strong effect on magnetism, while for the coarser configurations typically studied by microscopy
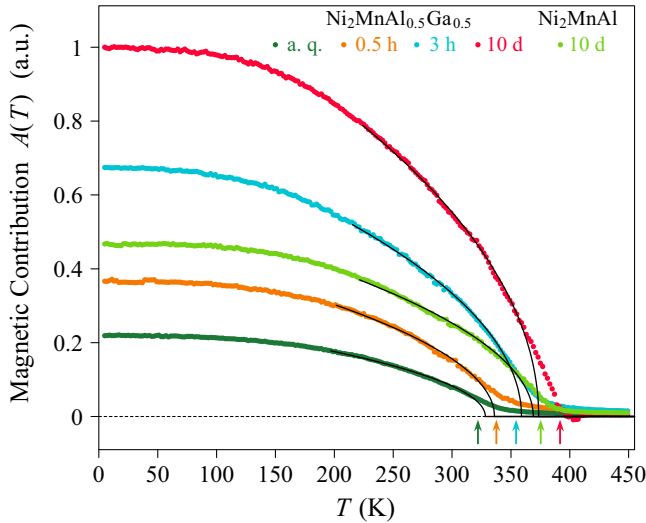
FIG. 6. Decrease of the magnetic contribution in the SANS profiles with increasing temperature. The positions of the magnetic transition temperatures $T_c$ according to DSC are marked by arrows, while a fitted mean-field critical behavior $\sqrt{1 - (T/T_c)}$ is depicted as black solid lines.

[7,12,13], secondary effects such as magnetostatics can become more important.

To study the evolution of the magnetic domain signal with temperature we consider the fitted prefactor of the magnetic signal $A(T)$ according to Eq. (3), which is proportional to the total magnetic small-angle scattering of the sample and thus, assuming each sample to comprise an equal number of formula units, to the ordered magnetic moment per formula unit. Figure 6 depicts these values relative to the strength of the magnetic contribution of the $Ni_2MnAl_{0.5}Ga_{0.5}$ sample with a 10 d annealing duration measured at 5 K. We observe a continuous decrease of the magnetic signal with increasing temperature, consistent with the expected second-order phase transition. For a simple determination of the magnetic transition temperatures, we fit the signals with the critical behavior $\sqrt{1 - (T/T_c)}$ according to mean-field theory. The corresponding phase-transition temperatures agree well with those obtained via DSC on the respective samples, with the remaining deviations being probably due to the broad DSC signal of the powder samples and the resulting ambiguity in defining the transition temperature as mentioned in Sec. III.

With annealing, the magnetic small-angle scattering steadily increases for $Ni_2MnAl_{0.5}Ga_{0.5}$ (and also for $Ni_2MnAl$, where the scattering in the as-quenched state is essentially zero according to Fig. 5). This is in apparent contrast to the growth of the characteristic lengths $L_{struc}$ and $L_{mag}$, where only after 10 d annealing a significant increase is visible. We rationalize these observations in the following way: The coarsening kinetics show a thermally activated behavior. Thus, when quenching the sample from the disordered state to room temperature, the few moments the sample spends just below the ordering temperature (931 K for $Ni_2MnAl_{0.5}Ga_{0.5}$ [15]) will coarsen the configuration to a scale that would have taken much longer to reach at the low-temperature annealing temperature of 623 K. However, the resulting degree of long-

range order corresponds to the equilibrium value just below the order-disorder transition and is thus quite low. Consequently, the ordered moment per formula unit is small, as a Mn antistructure atom aligns antiparallel to the regular Mn spins [11]. At subsequent low-temperature annealing, first the degree of long-range order within the existing APDs increases towards the new equilibrium value, taking a few atomic exchanges per site, which apparently corresponds to timescales of some hours as probed by our first annealing steps. Only on much longer timescales on the order of days does significant APD coarsening happen.

We also want to note that, even assuming our hypothesis of APD boundaries inducing domains in the magnetic ground state, which justifies our use of the model function describing structural domain scattering also for the magnetic SANS signal, deviations around the magnetic transition could be expected. Due to the APD boundaries, the interaction of the spins is spatially inhomogeneous, and thus the "local" magnetic transition temperature could be different within the domains and at the boundaries. Note that in particular for Mn segregation to the APD boundaries, it is well conceivable that the domain boundaries can keep their magnetic order to higher temperatures, leading to a peculiar state of two-dimensional magnetically ordered interfaces separating paramagnetic domains, while the converse scenario would lead to a loss of magnetic order towards the boundaries. In either case, the additional structure in the local magnetization around the phase transition would affect the shape of the SANS signal. As our data can be well described at all temperatures by the combination of short-range ordered paramagnetic scattering and the domain signal with a temperature-independent scale, we can conclude that such effects, which in principle should be expected to occur, are not strong.

Finally, we want to discuss the relevance of our work for general Mn-based Heusler materials, beyond the specific systems considered here. We are aware of another SANS investigation on spatially inhomogeneous magnetism in the composition series $Ni_{50-x}Co_xMn_{40}Sn_{10}$. In the pertinent publications [21,37] the authors similarly observed a shoulder in the magnetic SANS signal around 0.3 nm$^{-1}$, but gave an interpretation in terms of ferromagnetically ordered clusters of spins embedded in a nonferromagnetic matrix (or alternatively within a matrix of smaller magnetization). It has to be conceded that their system presents a more complicated situation, hosting a martensitic phase and having a tendency for chemical phase separation [37], but we want to raise the possibility of APD-induced magnetic domains also for this case: for the ternary end member $Ni_{50}Mn_{40}Sn_{10}$ the $L2_1$ ordering temperature has been reported to be close to 900 K [38], which is even somewhat lower than the 931 K for our $Ni_2MnAl_{0.5}Ga_{0.5}$ already quoted above. Thus, a priori it has to be assumed that quenched $Ni_{50-x}Co_xMn_{40}Sn_{10}$ will have antiphase domains on the same scale as in our study, and their role in explaining magnetic spatial inhomogeneities should be considered.

## VI. CONCLUSION

We have studied the relation between structural and magnetic order in $Ni_2MnAl$ and $Ni_2MnAl_{0.5}Ga_{0.5}$ powder samples

of distinct L2$_1$ order states by neutron powder diffraction and small-angle neutron scattering, respectively. Applying a phenomenological model derived from simulations of the coarsening of APDs allowed us to extract the respective correlation lengths in a rigorous way. Their coupled variation over the distinct samples, as well as their quantitative closeness are strong arguments that magnetic domain walls are not only pinned at antiphase domain boundaries, but that structural domain boundaries inherently induce magnetic domain boundaries in these systems, and thus that structural and magnetic domain configurations are essentially identical.

The reason for the observed behavior lies clearly in the strongly distance-dependent interaction between Mn spins, which are principally responsible for magnetism in these systems, corresponding to a mechanism that is fundamentally different from the competition between short-range exchange interaction and long-range dipole-dipole interaction that gives rise to Weiss' domains. These induced magnetic domain boundaries will show a much stronger resilience against external magnetic fields than conventional magnetic domain walls

and thus likely be responsible for the increased magnetic stiffness and reduced achievable magnetization of samples at early annealing stages with fine-grained antiphase domain configurations, constituting an alternative way of how structural order can affect the magnetic behavior beyond the effect of the degree of long-range order. The described mechanism is clearly generally applicable, but our findings are of particular relevance for the widely investigated class of Heusler systems with Mn as the dominant magnetic species, where in future investigations the antiphase domain scale should be regarded as an additional parameter to be controlled when considering the magnetic properties.

[1] N. S. Stoloff, Int. Metals Rev. **29**, 123 (1984).

[2] T. Graf, C. Felser, and S. S. P. Parkin, Prog. Solid State Chem. **39**, 1 (2011).

[3] H. Zijlstra and H. B. Haanstra, J. Appl. Phys. **37**, 2853 (1966).

[4] M. Acet, E. Duman, E. F. Wassermann, L. Mañosa, and A. Planes, J. Appl. Phys. **92**, 3867 (2002).

[5] P. Neibecker, M. E. Gruner, X. Xu, R. Kainuma, W. Petry, R. Pentcheva, and M. Leitner, Phys. Rev. B **96**, 165131 (2017).

[6] A. J. Lapworth and J. P. Jakubovics, Philos. Mag. (1798–1977) **29**, 253 (1974).

[7] S. P. Venkateswaran, N. T. Nuhfer, and M. De Graef, Acta Mater. **55**, 2621 (2007).

[8] T. Asaka, X. Z. Yu, Y. Tomioka, Y. Kaneko, T. Nagai, K. Kimoto, K. Ishizuka, Y. Tokura, and Y. Matsui, Phys. Rev. B **75**, 184440 (2007).

[9] P. J. Webster, K. R. A. Ziebeck, S. L. Town, and M. S. Peak, Philos. Mag. B **49**, 295 (1984).

[10] K. R. A. Ziebeck and P. J. Webster, J. Phys. F: Met. Phys. **5**, 1756 (1975).

[11] E. Simon, J. G. Vida, S. Khmelevskyi, and L. Szunyogh, Phys. Rev. B **92**, 054438 (2015).

[12] T. Yano, Y. Murakami, R. Kainuma, and D. Shindo, Mater. Trans. **48**, 2636 (2007).

[13] Y. Murakami, T. Yano, R. Y. Umetsu, R. Kainuma, and D. Shindo, Scr. Mater. **65**, 895 (2011).

[14] H. S. Park, Y. Murakami, K. Yanagisawa, T. Matsuda, R. Kainuma, D. Shindo, and A. Tonomura, Adv. Funct. Mater. **22**, 3434 (2012).

[15] H. Ishikawa, R. Y. Umetsu, K. Kobayashi, A. Fujita, R. Kainuma, and K. Ishida, Acta Mater. **56**, 4789 (2008).

[16] R. Y. Umetsu, H. Ishikawa, K. Kobayashi, A. Fujita, K. Ishida, and R. Kainuma, Scr. Mater. **65**, 41 (2011).

[17] D. Craik and R. Tebble, Rep. Prog. Phys. **24**, 116 (1961).

[18] A. Budruk, C. Phatak, A. K. Petford-Long, and M. De Graef, Acta Mater. **59**, 4895 (2011).

[19] L. Straka, L. Fekete, and O. Heczko, Appl. Phys. Lett. **113**, 172901 (2018).

[20] P. Scherrer, Nachr. Ges. Wiss. Göttingen Math.-Phys. Kl. **1918**, 98 (1918).

[21] K. P. Bhatti, S. El-Khatib, V. Srivastava, R. D. James, and C. Leighton, Phys. Rev. B **85**, 134450 (2012).

[22] G. Benacchio, I. Titov, A. Malyeyev, I. Peral, M. Bersweiler, P. Bender, D. Mettus, D. Honecker, E. P. Gilbert, M. Coduri, A. Heinemann, S. Mühlbauer, A. Çakır, M. Acet, and A. Michels, Phys. Rev. B **99**, 184422 (2019).

[23] S. Mühlbauer, D. Honecker, E. A. Périgo, F. Bergner, S. Disch, A. Heinemann, S. Erokhin, D. Berkov, C. Leighton, M. R. Eskildsen, and A. Michels, Rev. Mod. Phys. **91**, 015004 (2019).

[24] R. W. Overholser, M. Wuttig, and D. A. Neumann, Scr. Mater. **40**, 1095 (1999).

[25] J. Sołtys, Phys. Status Solidi A **66**, 485 (1981).

[26] R. Kainuma, M. Ise, K. Ishikawa, I. Ohnuma, and K. Ishida, J. Alloys Compd. **269**, 173 (1998).

[27] Y. Sutou, I. Ohnuma, I. Kainuma, and K. Ishida, Metall. Mater. Trans. A **29**, 2225 (1998).

[28] P. Neibecker, M. Leitner, G. Benka, and W. Petry, Appl. Phys. Lett. **105**, 261904 (2014).

[29] A. Huq, M. Kirkham, P. F. Peterson, J. P. Hodges, P. S. Whitfield, K. Page, T. Hugle, E. B. Iverson, A. Parizzi, and G. Rennich, J. Appl. Crystallogr. **52**, 1189 (2019).

[30] G. S. Pawley, J. Appl. Crystallogr. **14**, 357 (1981).

[31] R. B. Von Dreele, J. D. Jorgensen, and C. G. Windsor, J. Appl. Crystallogr. **15**, 581 (1982).

[32] U. Zweck and M. Leitner, Phys. Rev. B **104**, 094101 (2021).

[33] C. S. Smith and L. Guttman, J. Met. **5**, 81 (1953).

[34] S. Mühlbauer, A. Heinemann, A. Wilhelm, L. Karge, A. Ostermann, I. Defendi, A. Schreyer, W. Petry, and R. Gilles, Nucl. Instrum. Methods Phys. Res., Sect. A **832**, 297 (2016).

[35] A. Heinemann and S. Mühlbauer, J. Large-Scale Res. Facil. **1**, A10 (2015).

[36] G. Porod, Kolloid-Z. **124**, 83 (1951).

[37] S. El-Khatib, K. P. Bhatti, V. Srivastava, R. D. James, and C. Leighton, Phys. Rev. Mater. **3**, 104413 (2019).

[38] E. Wachtel, F. Henninger, and B. Predel, J. Magn. Magn. Mater. **38**, 305 (1983).